Impact of sea ice cover changes on the Northern Hemisphere atmospheric winter circulation

By R. JAISER[1]*, K. DETHLOFF[1], D. HANDORF[1], A. RINKE[1] AND J. COHEN[2],

[1]*Alfred Wegener Institute for Polar and Marine Research, Research Unit Potsdam, D-14473 Potsdam, Telegrafenberg A43, Germany*; [2]*Atmospheric and Environmental Research, Inc., 131, Hartwell Avenue, Lexington, MA 02421, USA*

ABSTRACT

The response of the Arctic atmosphere to low and high sea ice concentration phases based on European Center for Medium-Range Weather Forecast (ECMWF) Re-Analysis Interim (ERA-Interim) atmospheric data and Hadley Centre's sea ice dataset (HadISST1) from 1989 until 2010 has been studied. Time slices of winter atmospheric circulation with high (1990–2000) and low (2001–2010) sea ice concentration in the preceding August/September have been analysed with respect to tropospheric interactions between planetary and baroclinic waves. It is shown that a changed sea ice concentration over the Arctic Ocean impacts differently the development of synoptic and planetary atmospheric circulation systems. During the low ice phase, stronger heat release to the atmosphere over the Arctic Ocean reduces the atmospheric vertical static stability. This leads to an earlier onset of baroclinic instability that further modulates the non-linear interactions between baroclinic wave energy fluxes on time scales of 2.5–6 d and planetary scales of 10–90 d. Our analysis suggests that Arctic sea ice concentration changes exert a remote impact on the large-scale atmospheric circulation during winter, exhibiting a barotropic structure with similar patterns of pressure anomalies at the surface and in the mid-troposphere. These are connected to pronounced planetary wave train changes notably over the North Pacific.

Keywords: Arctic sea ice; atmospheric circulation; baroclinic-planetary interactions; teleconnections

1. Introduction

The observed decrease in Arctic summer sea ice cover over recent decades is likely due to a combination of decadal-scale variability in the coupled ice–ocean–atmosphere–land system and radiative greenhouse gas forcing (Serreze et al., 2007). Stroeve et al. (2007) analysed the Arctic sea ice cover changes in the Fourth IPCC Assessment Report model simulations and demonstrated that the observed sea ice retreat is much faster than in the model mean. This shows a deficit in reproducing the underlying processes for the observed Arctic sea ice decline in most of the models and may indicate that the mechanisms are not completely understood.

Arctic sea ice is an important component in the global climate system. One reason is that the amount of ice regulates heat exchange between the cold atmosphere and the warmer, ice-covered ocean in winter. In recent Septembers, Arctic sea ice retreated extensively leading to large areas of thin first-year ice during the freeze up season that are more vulnerable to melting out in summer (Stroeve et al., 2011b). Furthermore, changes in sea ice interact with dynamical processes related to changes in atmospheric wind and temperature fields, ocean currents and heat storage as well as to thermodynamic and radiative processes connected with water vapour, clouds and aerosol feedbacks (see review by Budikova, 2009). Blanchard-Wrigglesworth et al. (2011) investigated the temporal and memory effects of sea ice and showed on the basis of model simulations and observations that Arctic sea ice de-correlates over a time scale of 2–5 months with longer persistence times in winter and summer.

A large amount of the recently observed sea ice retreat is linked to changes in atmospheric circulation and teleconnection patterns associated with the North Atlantic oscillation/Arctic oscillation (NAO/AO), and its shift to a stronger positive phase during the early 1990s (Rigor et al., 2002). The mean impact of sea ice anomalies on the atmospheric circulation has been investigated by

---

*Corresponding author.
email: Ralf.Jaiser@awi.de

1

Gerdes (2006), Deser et al. (2007), Liu and Alexander (2007), Francis et al. (2009), Overland and Wang (2010) and Petoukhov and Semenov (2010). Their results suggest that Arctic sea ice influences the formation of mid-latitude teleconnection patterns and especially the NAO mode. Over the Atlantic Ocean and the European continent, the large-scale atmospheric response to Arctic sea ice cover variations is most significant in the free troposphere and resembles the internal mode of atmospheric variability, the NAO/AO and reaches equilibrium 2–2.5 months after the initial sea ice cover change (Deser et al., 2007).

Dethloff et al. (2006) argued that the impact of changes in sea ice and snow cover on the atmospheric circulation is stronger in the Pacific than in the Atlantic sector because the related changes in the Arctic energy balance generate a large-scale atmospheric wave train across the Pacific basin. Modelled atmospheric responses to sea ice variability across the Pacific basin resemble observed data as demonstrated by Honda et al. (1996). They suggested that the ice–atmosphere interaction in the North Pacific sector differs from that in the North Atlantic sector by enhancing the original atmospheric circulation anomaly and by exerting a positive feedback on the large-scale atmospheric circulation.

Sempf et al. (2005) showed in an idealised model of the Northern Hemisphere's wintertime atmospheric circulation that the zonally asymmetric pattern of the AO mode is a result of thermal land–sea contrasts and topography, connected with the regionalisation of transient baroclinic activity.

Here, we study the connection between atmospheric planetary waves and baroclinic cyclonic systems in winter, both influenced by Arctic heat anomalies in autumn following low sea ice concentrations and their impact on large-scale circulation changes. This study benefits from the improved quality of the European Center for Medium-Range Weather Forecast (ECMWF) Re-Analysis Interim (ERA-Interim) dataset in the Arctic, which we apply here.

The processes that link low Arctic sea ice extent in autumn with hemispheric winter circulation anomalies associated with atmospheric teleconnection patterns are not well understood. More research is needed to explore the relative contribution of Arctic sea ice cover changes to the atmospheric planetary waves and the non-linear interactions with transient baroclinic activity. As shown by Sempf et al. (2007), these interactions are the main drivers for seasonal and decadal-scale changes between positive and negative AO phases, which can be considered as atmospheric flow regimes resulting from chaotic wandering of the trajectories in phase space on the ruins of merged attractors.

Screen and Simmonds (2010) identified an amplified Arctic warming above 700 hPa in the ERA-Interim dataset, which appears during winter and is consistently weaker than the near-surface warming. The existence of the amplified tropospheric warming requires that, in addition to the increased transfer of heat from the ocean to the atmosphere resulting from sea ice loss, other dynamical processes play an important role in winter. Graversen et al. (2008a) examined the vertical structure of temperature change in the Arctic during the late–20th-century using ERA-40 data. They found a temperature amplification above the surface and concluded that changes in meridional atmospheric heat transport may be an important driver for the recent Arctic temperature amplification. These findings have been largely discussed and confirmed by the Japanese 25-year Re-Analysis (JRA-25) and satellite observations (Graversen et al., 2008b). Nevertheless, Screen and Simmonds (2011) documented a discontinuity in the ERA-40 dataset, which makes its use for determination of Arctic temperature trends problematic.

Using more recent ERA-Interim data, we analyse the influence of Arctic sea ice on transient baroclinic activity and large-scale atmospheric circulation systems and their non-linear interactions during the winter season for a period with high ice concentration (1990–2000) and a period of low ice concentration (2001–2010). By diagnosing the non-linear connections between the Arctic sea ice cover, planetary waves and synoptic storm tracks during winter, the influence of sea ice concentration changes on atmospheric circulation changes has been identified. A main focus is on the scale separation between planetary waves and synoptic-scale changes during the atmospheric adjustment process with respect to high and low sea ice cover changes. The results of this observational study are compared with a model study reported by Sokolova et al. (2007), where two time slices with high and low sea ice cover have been analysed with respect to the non-linear atmospheric interactions between planetary and baroclinic waves. They found an increase in Eliassen-Palm (EP) fluxes on baroclinic scales, a decrease in planetary scales and preferred positive AO phases for high ice regimes.

2. Data and analysis

The analysis has been carried out using the ECMWF ERA-Interim data, which is described by Dee and Uppala (2009). This dataset has an improved atmospheric model and assimilation system, which replaces that used in ERA-40, particularly for the data-rich 1990s and 2000s. Main improvements over the ERA-40 dataset include higher spectral resolution at T255, improved model physical parameterisations, a better hydrological cycle, four-dimensional variational data assimilation and variational bias correction of satellite radiance data (Dee and Uppala, 2009). ERA-Interim data deliver more realistic

Arctic tropospheric temperatures as described by Screen and Simmonds (2010) and reduced biases in the Arctic region (Dee and Uppala, 2009).

For our study, we use daily ERA-Interim data on a $2° \times 2°$ latitude/longitude grid with the seasonal cycle removed. The variables analysed include atmospheric temperature, wind, geopotential heights and mean sea level pressure. Changes in baroclinic and planetary-scale fluxes are considered separately. Therefore, two digital filters are used with weights developed by Blackmon and Lau (1980). Baroclinic-scale fluctuations are extracted by a band-pass filter sensitive to time periods between 2.5 and 6 days. For planetary-scale fluctuations, a low-pass filter is used sensitive to time periods larger than 10 days. The latter one is limited to 90 days, given that the seasonal cycle has been removed. With the resulting filtered data, we further calculate heat and momentum fluxes and the localised EP flux vector (see Appendix for details) introduced by Trenberth (1986). These fluxes are used to diagnose the wave activity in the troposphere and the stratosphere. Furthermore, the divergence of the EP flux describes the impact of planetary or baroclinic-scale disturbances on the time mean flow.

In addition to atmospheric data, we use monthly sea ice concentration data taken from the Met Office Hadley Centre's sea ice and sea surface temperature dataset (HadISST1, Rayner et al., 2003) on a $1° \times 1°$ latitude/longitude grid. In Fig. 1, we show the standard deviation of sea ice concentration for August/September 2001–2010. We calculated an area mean of sea ice concentration for the Siberian domain, including the Kara, Laptev and East Siberian Seas ($83°$–$75°$ N, $60°$–$180°$ E, delineated by the blue line in Fig. 1) and averaged it over August and September. The region is chosen because of large sea ice variability and a strong impact on atmospheric systems as discussed by Honda et al. (2009). The result is a time series with one value for each year forming a sea ice concentration index. This late summer ice index is correlated with the above-mentioned atmospheric data averaged for the winter season (December to February, DJF). Significance of correlations is computed using a Student's t-test with a 90% confidence level.

For our sensitivity studies, we selected two consecutive winter periods 1990–2000 and 2001–2010. The first 11-year period, 1990–2000, is chosen as a time slice with significantly larger sea ice concentration in the preceding late summer (with a mean value in the Siberian domain of 0.57), referred to as the high ice phase. The second 10-year period, 2001–2010, represents less sea ice concentration (mean value of 0.45), referred to as the low ice phase. Differences in the atmospheric data between both phases are investigated for significance using a Student's t-test with 90% confidence level.
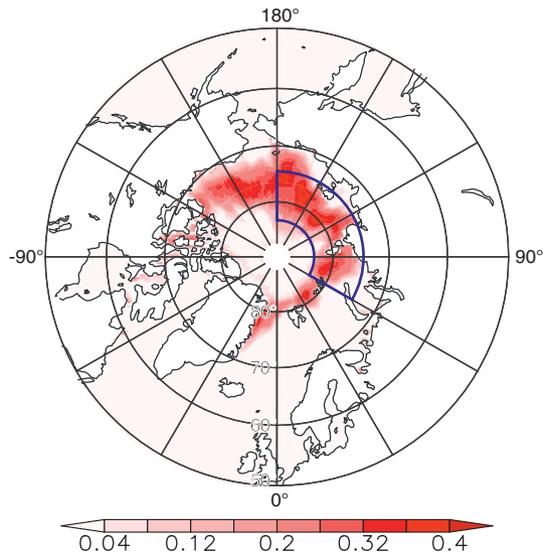

Fig. 1. Standard deviation of late summer HadISST1 sea ice concentration August/September (2001–2010) and the Siberian domain (blue) used in correlations of atmospheric variables with sea ice concentration.

A maximum covariance analysis (MCA; von Storch and Zwiers, 1999, see Appendix for details) is used to describe the relation between the fields of averaged August/September sea ice concentration and mean sea level pressure or 500 hPa geopotential heights in the consecutive autumn or winter over the whole time period 1989–2010. The results of this analysis method are pairs of patterns and associated time series for each climatic field, which are coupled through a maximised co-variance of their associated time series. The figures show the pairs of patterns that are expected to occur simultaneously.

3. Impact of sea ice cover on the atmosphere

The winter 500 hPa geopotential differences between low and high ice concentration in Fig. 2a exhibit pronounced changes over high and middle latitudes. The lower/higher values of geopotential heights over the Arctic Ocean are associated with higher/lower sea ice concentration during the analysed period. In contrast, positive/negative geopotential anomalies are observed over the Atlantic and Pacific Oceans during the high/low ice phase. Similar changes in the mean sea level pressure fields between both periods are shown in Fig. 2b consistent with the more frequent occurrence of negative AO pattern in the later period.

To understand the linkage between low Arctic sea ice extent in August/September with these observed atmospheric circulation anomalies in winter, we first focus on the baroclinic interactions during autumn. Figure 3 shows two sets of coupled patterns obtained by the MCA of ice
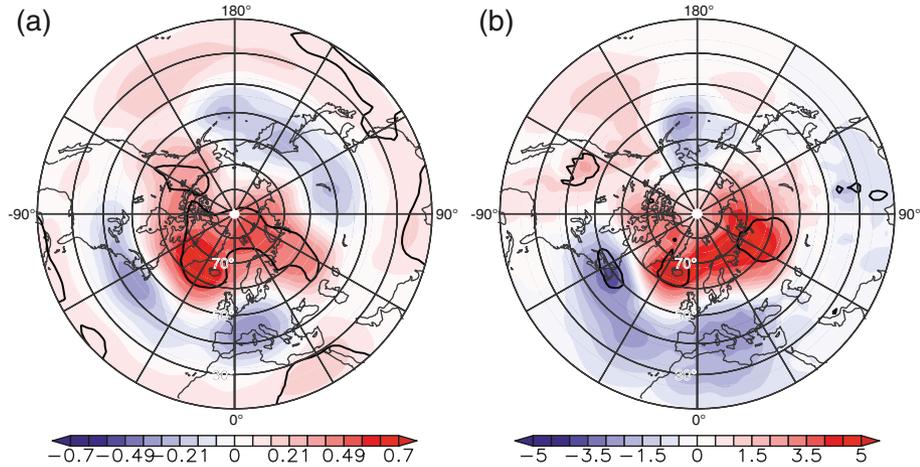
Fig. 2. (a) ERA-Interim 500 hPa geopotential height differences (10^3 gpm) between low (2001–2010) and high (1990–2000) ice phases for winter (DJF), (b) same for mean sea level pressure (hPa). Statistical significance with a 90% confidence level is delineated by black contour.

concentration in August/September with sea level pressure and geopotential height fields in autumn (September to November, SON), respectively. For each analysis, the first two pairs of MCA patterns are displayed. September sea ice/September sea ice concentration with sea level pressure (SLP) (Fig. 3a–d) the first pair of MCA patterns (explaining 29% of co-variance) describes diminishing sea ice especially over the Siberian and Beaufort Sea covarying with positive pressure anomalies over the North Atlantic and negative pressure anomalies over North Siberia. The second MCA patterns (explaining 16% of co-variance) reveal an east–west dipole in sea ice variability over the Siberian and

Beaufort Sea, which is related to one centre of pressure anomalies over the Eastern Arctic and a reversed centre over the northern North Pacific.

The MCA of averaged August/September sea ice concentration with geopotential height at 500 hPa is shown in Fig. 3e–h. The first MCA patterns (explaining 35% of co-variance) again describe diminishing sea ice especially over the Siberian and Beaufort Sea covarying with positive height anomalies over the Arctic Ocean extending to eastern Europe and central Canada, respectively, and a negative anomaly close to the Aleutian Islands. The second MCA patterns (explaining 16% of co-variance) reveal
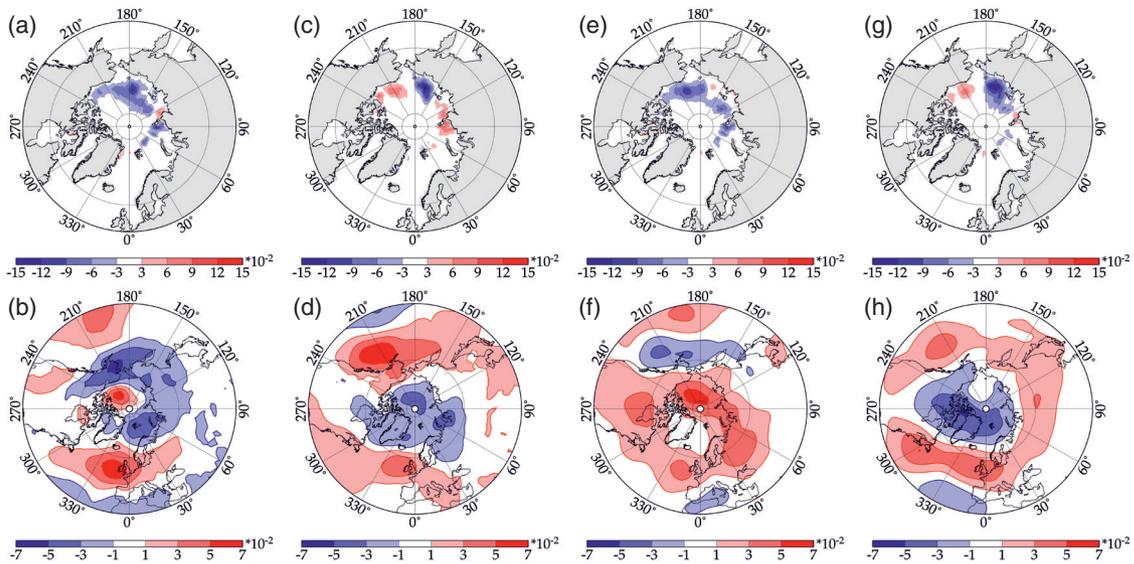

Fig. 3. First (a, b and e, f) and second pair (c, d and g, h) of coupled patterns obtained by the maximum covariance analysis (MCA) of HadISST1 sea ice concentration in August/September with ERA-Interim sea level pressure and 500 hPa geopotential height fields in autumn (SON) 1989–2010. Upper row displays the sea ice concentration anomaly maps. Lower row contains the corresponding anomaly maps for mean sea level pressure (b, d) and 500 hPa geopotential heights (f, h).

again an east–west dipole in sea ice variability over the Siberian and Beaufort Sea, which is associated with one centre of height anomalies over the winter Arctic Ocean, and a reversed centre over the mid-latitudes of the North Atlantic and Eurasia.

In the first sets of coupled MCA patterns between sea ice concentration and sea level pressure or 500 hPa geopotential heights, respectively, the anomaly patterns of sea ice (compare Fig. 3a and e) show similar structures. In contrast the anomaly patterns of sea level pressure (Fig. 3b) and geopotential height at 500 hPa (Fig. 3f) have little similarity. These differences between the surface and 500 hPa indicate a pronounced baroclinic response of the atmosphere to reduced sea ice concentration in autumn.

To illustrate the importance of baroclinic processes, we show height-time cross sections of the vertical static stability, Eady growth rates and meridional heat fluxes on time scales 2.5–6 days in Fig. 4 from September to December for the low ice and high ice phase. Eady growth rates have been computed as described in the study by Lindzen and Farrell (1980). The Eady growth rate measures changes in the baroclinicity using changes in atmospheric stability and the meridional temperature gradient (see Appendix for details). Values of the respective variable are plotted, averaged over the Siberian domain for high and low ice phase, respectively. In Fig. 4a for the high ice period as well as in Fig. 4b for the low ice period the increase of vertical static stability in the low atmosphere in late October can be seen. Comparing both figures, a decrease in atmospheric stability during the low ice period is visible. The difference plot (Fig. 4c) shows this reduction in the middle and lower troposphere in autumn continuing until December. Eady growth rates are larger in autumn compared to winter as seen in Fig. 4d and e. Furthermore,
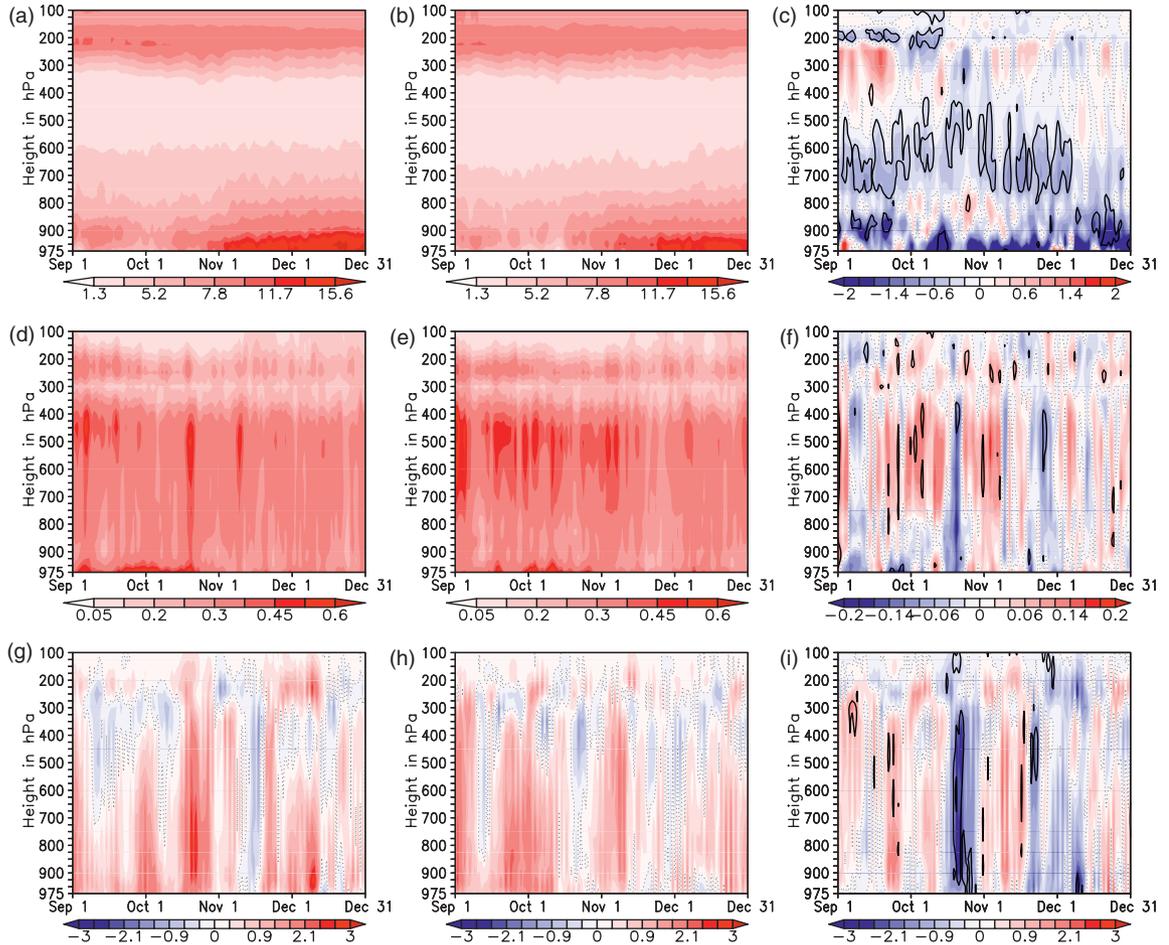

Fig. 4. Height–time cross sections of ERA-Interim data averaged over the Siberian domain. (a–c) static stability (10^{-3} km^{-1}), (d–f) Eady growth rates (day^{-1}) and (g–i) meridional heat flux (Kms^{-1}) on baroclinic time scales (2.5–6 days) for September–December for (a, d, g) 1989–1999, (b, e, h) 2000–2009 and (c, f, i) as difference of 2000–2009 minus 1989–1999. Statistical significance with a 90% confidence level is delineated by black contour.

they are increased in the low ice period (Fig. 4e). This is partly due to decreased atmospheric stability and therefore baroclinicity rises in the later period. Fig. 4f shows this increase beginning in late September continuing to November. Meridional baroclinic heat fluxes are enhanced around the beginning of October as seen by comparing Fig. 4g and h. The difference plot in Fig. 4i describes stronger meridional baroclinic heat fluxes until mid-October during the low sea ice phases. The large negative difference in the second half of October results from stronger heat fluxes in the high ice period in coincidence with weak heat fluxes in the low ice period. This heat flux burst with duration of approximately 1 week could be related to the passage of Arctic Cyclones. More detailed investigations similar to those of Inoue et al. (2010) are needed. As shown by Tietsche et al. (2011), additional oceanic heat uptake during summer is rapidly returned to the atmosphere during the following autumn. This heat release to the atmosphere in autumn is connected to an earlier onset of baroclinic instability because of static stability and Eady growth rate changes during the low ice phase.

To understand the atmospheric winter response to sea ice anomalies in late summer, Fig. 5a displays the correlation of the over all longitudes zonally averaged temperature in winter of the last decade 2001–2010 with sea ice concentration in the Siberian domain in the preceding late summer. There are only weak correlations in the high ice period 1989–1999 because the August/September sea ice concentration variability is low. Low sea ice concentration is associated with higher temperatures in the lower troposphere in the polar region (65°–80° N) peaking at 75° N (indicated by a negative correlation). The temperature increase, which is in agreement with Screen and Simmonds (2010), reduces the vertical static stability of the lower Arctic atmosphere. Francis et al. (2009) got a similar result using National

Centers for Environmental Prediction (NCEP) reanalysis data from 1979 until 2007 and showed that the Arctic atmosphere remembers the summer sea ice concentration reduction through a warming and de-stabilisation of the lower troposphere. The positive correlation between vertical static stability and sea ice concentration in the Siberian domain (Fig. 5b) demonstrates that reduced vertical stability is connected with less sea ice concentration. Because the onset of baroclinic instability is proportional to the strength of the vertical static stability of the atmosphere, reduced stability leads to an earlier onset of unstable baroclinic systems in the Arctic troposphere. To examine the impact on baroclinic systems in more detail, we plot in Fig. 5c the correlation between winter Eady growth rate and late summer sea ice concentration in the Siberian domain. The effect of the changed meridional temperature gradient dominates. The correlation indicates an enhanced baroclinicity north of 75° N in winter for less sea ice in summer, whereas the Eady growth rate between 60° and 70° N is decreased. This may indicate a shift in the occurrence of storms and cyclones to the north. Stroeve et al. (2011a) analysed the JRA-25 atmospheric dataset and detected a shift towards stronger and more frequently occurring cyclones in the Atlantic sector of the Arctic.

In Fig. 6a, we present the correlation of winter meridional heat fluxes on time scales from 2.5 to 6 days with sea ice concentration in the Siberian domain for the high ice phase and in Fig. 6c for the low ice phase. Stronger baroclinic heat fluxes in the latter period are connected with reduced sea ice concentration. This is indicated by statistically significant negative correlations in the whole Arctic troposphere with a maximum between 75° and 85° N above the surface and between 500 and 400 hPa. In Fig. 6, we further present the respective correlation of transient meridional heat fluxes on time scales from 10 to 90 days
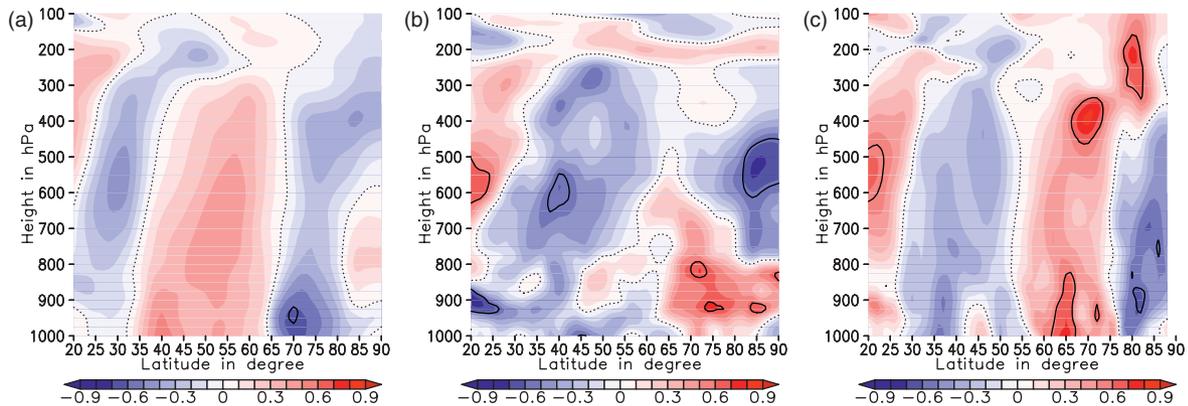

Fig. 5. Correlation coefficients of winter (DJF) 2001–2010 atmospheric ERA-Interim data with preceding late summer (AS) HadISST1 sea ice concentration in the Siberian domain. Zonally averaged (a) temperature, (b) vertical static stability and (c) Eady growth rates. Statistical significance with a 90% confidence level is delineated by black contour.
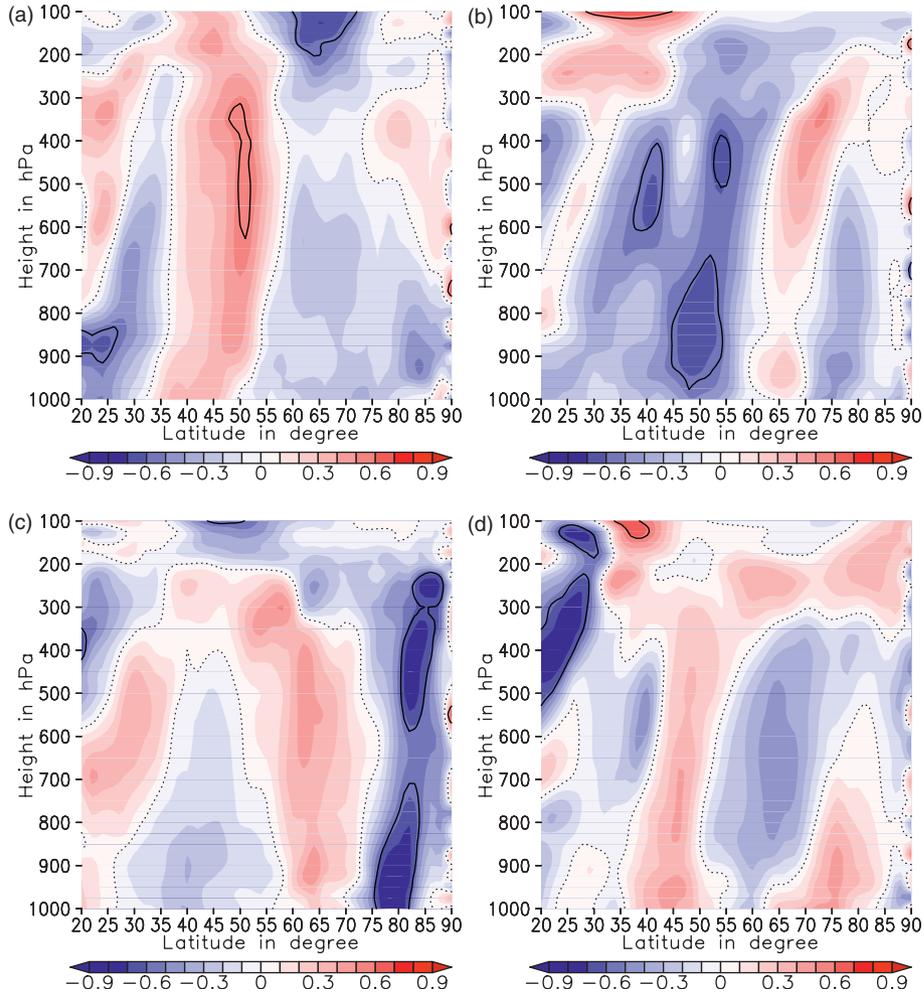
Fig. 6. Correlation coefficients of winter (DJF) ERA-Interim transient meridional heat fluxes with preceding late summer (AS) HadISST1 sea ice concentration in the Siberian domain. (a) Baroclinic scales (2.5–6 days) 1990–2000, (b) planetary scales (10–90 days) 1990–2000, (c) baroclinic scales (2.5–6 days) 2001–2010 and (d) planetary scales (10–90 days) 2001–2010. Statistical significance with a 90% confidence level is delineated by black contour.

with sea ice concentration for the high ice phase (Fig. 6b) and low ice phase (Fig. 6d). The correlation with sea ice concentration in the Siberian domain for the low ice phase is positive in the lower Arctic troposphere between 70° and 85° N. Reduced heat fluxes due to planetary waves are connected with reduced ice concentration and thus show an inverse behaviour compared to the baroclinic heat fluxes at the same latitude band. The comparison of Figs. 6c and d demonstrates the compensating interactions between planetary and baroclinic heat fluxes with respect to sea ice concentration changes. This is in agreement with the study of Sokolova et al. (2007) based on a coupled atmosphere–ocean global climate model. Their analysis of two 7-year-long time slices with high and low ice showed similar compensating effects between baroclinic and planetary fluxes.

The impact of sea ice concentration changes on the planetary wave patterns on seasonal time scales has been additionally analysed by the zonally averaged localised EP fluxes. In Figs. 7a and b, we show the planetary heat and momentum fluxes on time scales from 10 to 90 days in the form of zonally averaged EP flux vectors and their magnitude for the high and the low sea ice phases. Differences are shown in Fig. 7c. Strongest changes between both decades are visible at high latitudes in the middle and high troposphere and lower stratosphere. Arctic EP fluxes caused by planetary waves are enhanced during the low sea ice phase as a result of the stronger diabatic heat source. The strongest planetary wave EP flux increase for low sea ice concentration occurs between 700 and 200 hPa in the latitudinal belt north of 65° N. This result based on ERA-Interim data is in qualitative
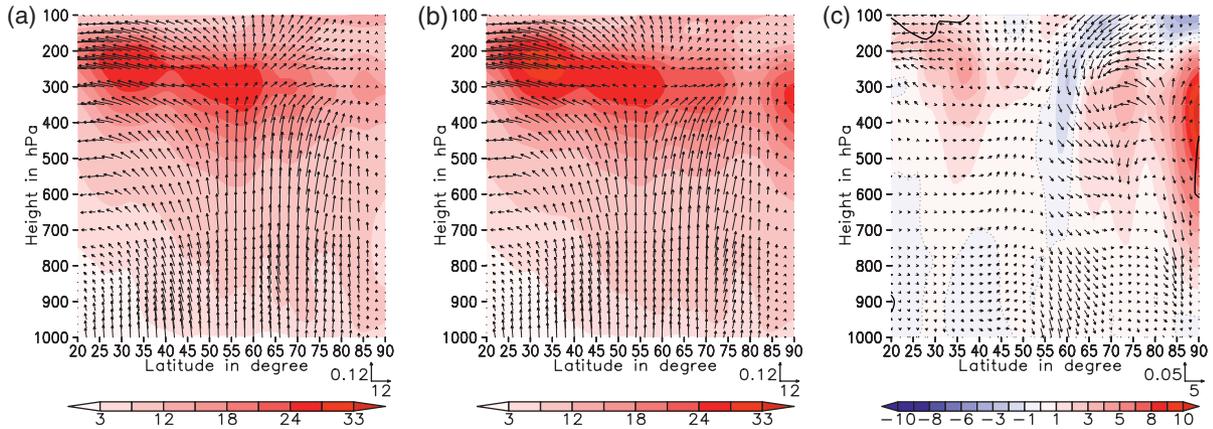
Fig. 7.   Winter (DJF) ERA-Interim EP flux vectors ($m^2 s^{-2}$) and their magnitude for time scales 10–90 days. (a) 1990–2000, (b) 2001–2010 and (c) differences 2001–2010 minus 1990–2000. Colours display the magnitude, arrows describe the EP vector propagation. Statistical significance with a 90% confidence level is delineated by black contour.

agreement with a similar analysis performed by Sokolova et al. (2007). Their experiments with a coupled climate model revealed positive planetary EP flux anomalies on seasonal time scales in a 7-year-long phase with low sea ice cover compared to a 7-year-long phase of higher sea ice cover.

Figure 8 displays the differences of the divergence of the EP flux on time scales from 10 to 90 days at 850, 500 and 200 hPa between the low and high sea ice time periods. A statistically significant planetary wave train over the Pacific Ocean connected to the topography of the Rocky Mountains in mid-latitudes is identified at all height levels, thus exhibiting a pronounced barotropic structure. A much weaker planetary wave train occurs over the Atlantic Ocean and Europe. This result based on ERA-Interim data is in qualitative agreement with the findings of different modelling studies, all showing a pronounced response in the North Pacific region. Dethloff et al. (2006) performed a sensitivity study with a coupled climate

model with improved Arctic snow cover and sea ice albedo parameterisations. Due to these changed surface forcings, a wave train in the EP flux over the Pacific Ocean occurred, similar to the results of the present study.

The baroclinic response of the large-scale atmospheric flow during autumn to sea ice anomalies in late summer (Fig. 3) changes to a hemispheric-wide barotropic response in winter that is not only visible in large-scale planetary waves (Fig. 8) but also in the response of the large-scale atmospheric flow during winter. The latter has been demonstrated again by the results of an MCA of ice concentration in August/September with sea level pressure and 500 hPa geopotential height fields in winter (DJF), as shown in Fig. 9.

For the MCA of August/September sea ice concentration with winter SLP (Fig. 9a–d), the first MCA patterns (explaining 58% of co-variance) describe diminishing sea ice especially over the Siberian and Beaufort Sea covarying with a pressure anomaly pattern resembling the negative
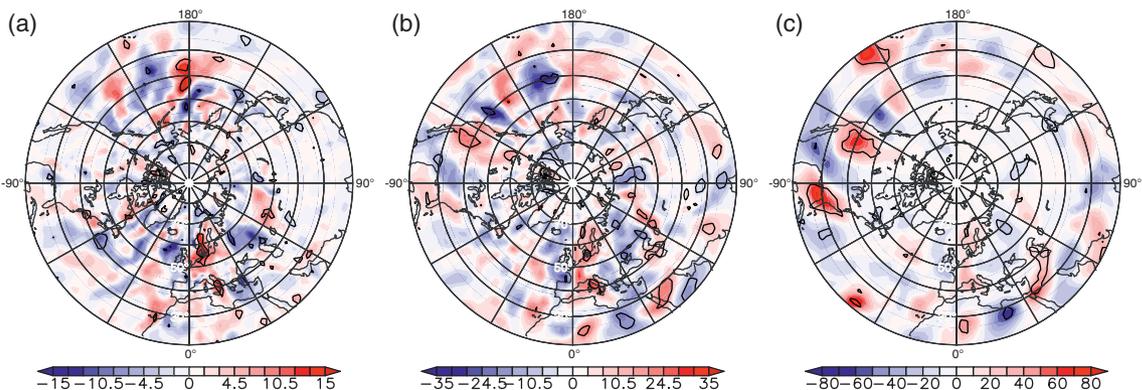

Fig. 8.   Divergence of winter (DJF) ERA-Interim EP-Fluxes (10^{-6} ms^{-2}) for time scales 10–90 days as difference (2001–2010) minus (1990–2000) (a) at 850 hPa, (b) 500 hPa and (c) 200 hPa. Statistical significance with a 90% confidence level is delineated by black contour.
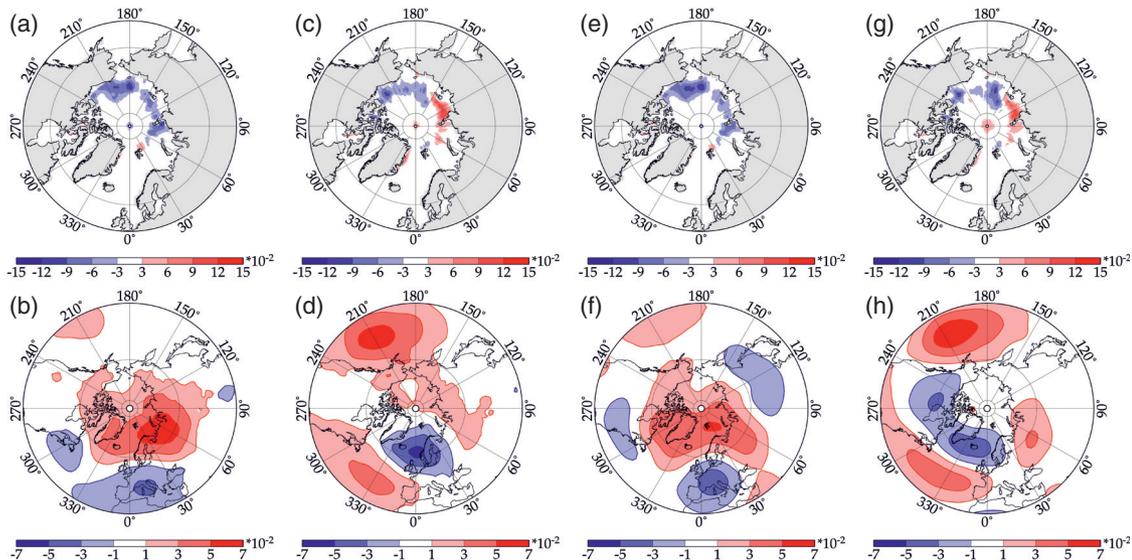
Fig. 9. First (a, b and e, f) and second pair (c, d and g, h) of coupled patterns obtained by the MCA of HadISST1 sea ice concentration in August/September with ERA-Interim sea level pressure and 500 hPa geopotential height fields in winter (DJF) 1989–2010. Upper row displays the sea ice concentration anomaly maps. Lower row contains the corresponding anomaly maps for mean sea level pressure (b, d) and 500 hPa geopotential heights (f, h).

phase of the NAO. The second MCA patterns (explaining 14% of co-variance) reveal an east–west dipole in sea ice variability over the Siberian and Beaufort Sea, which is related to a pronounced pressure anomaly over the northern North Pacific.

The coupled pairs of MCA patterns of August/September sea ice concentration with winter geopotential height at 500 hPa (Fig. 9e–h) resemble those of mean sea level pressure described above. This similarity indicates the barotropic response of the large-scale atmospheric winter circulation to sea ice anomalies in late summer.

The barotropic structure seen in the first coupled patterns of the MCA at the surface and in the middle troposphere, which is related to the diminishing sea ice (Fig. 9a, b, e and f), describes the same relation as between reduced sea ice concentration and negative AO phase in Fig. 2a and b. Accordingly, the MCA time series and the DJF AO-Index are correlated with a coefficient of –0.90 for sea level pressure and –0.80 for 500 hPa geopotential heights. This is in accordance with the results by Francis et al. (2009). The barotropic structure seen in the second coupled patterns of the MCA at the surface and in the middle troposphere displays the strongest atmospheric response over the northern North Pacific related to pronounced sea ice changes over the Siberian Sea (Fig. 9c, d, g and h) and corresponds to the area of the largest changes in planetary wave trains displayed in Fig. 8. Furthermore, the pattern of high and low pressure anomalies over the North Atlantic is connected to the NAO teleconnection pattern. The MCA time series and

the NAO-Index are, therefore, correlated with a coefficient of 0.72.

We showed that the initial response of the atmosphere to reduced sea ice concentration in late summer is baroclinic in autumn, which changes to barotropic in winter and triggers changes in the large-scale planetary wave trains over the Pacific. These findings are supported by Honda et al. (2009) who demonstrated in an atmosphere-only model that zonally propagating cold atmospheric anomalies from Europe to the Far East in late winter are correlated with the Arctic sea ice cover decrease in the preceding summer-to-autumn seasons.

4. Summary and conclusions

We showed that Arctic heating anomalies due to low sea ice concentrations in late summer (August/September) trigger changes in baroclinic systems in autumn because of an earlier onset of baroclinic instability that influences the structure of large-scale planetary waves in the following winter. The baroclinic structure of the direct response in autumn is linked to different patterns of pressure anomalies at the surface and in the mid-troposphere, which are related to the decrease in sea ice concentration. Decreased static stability and changed meridional temperature gradients induce an earlier onset of baroclinicity north of 75° N with greater amplitude.

Winter heat fluxes on baroclinic scales are increased in the whole Arctic troposphere, whereas a non-linear adjustment leads to decreased heat fluxes associated with

planetary waves. Arctic EP fluxes due to planetary waves during winter are enhanced between 700 and 200 hPa in the latitudinal belt north of $65°$ N during the low sea ice phase.

The barotropic structure of the atmospheric response in winter is connected to similar patterns of pressure anomalies at the surface and the mid-troposphere. The pattern over the North Atlantic relates the sea ice decline in late summer to a negative NAO phase in winter. The barotropic pattern over the Pacific due to changes in Arctic sea ice concentration is connected to a distinguished planetary wave train over the region.

These results deliver a dynamical background for understanding the role of Arctic sea ice decline on the Arctic temperature amplification and its impact on mid-latitudes contributing to the recent shift to the negative NAO phase. The reduced sea ice concentration at the end of the Arctic summer has the potential to change the large-scale circulation in the following winter that could feed back on the sea ice concentration. This sea ice–atmosphere relationship suggests a potential for use in operational Northern Hemisphere seasonal forecasts. Sea ice cover loss has the potential to preferentially shift the probability density function of the AO/NAO to the negative phase, in agreement with the investigations by Overland and Wang (2010).

The results of the present study showed the large influence of enhanced baroclinicity on planetary waves similar to the connection between snow cover anomalies and the large-scale atmospheric circulation as shown by Cohen et al. (2007). Further investigation is needed to examine the impact of enhanced baroclinic systems on snow anomalies in the Siberian region. It is plausible that both processes are closely related.

5. Acknowledgements

References

Blackmon, M. L. and Lau, N.-C. 1980. Regional characteristics of the Northern Hemisphere wintertime circulation: a comparison of the simulation of a GFDL general circulation model with observations. *J. Atmos. Sci.* **37**, 497–514.

Blanchard-Wrigglesworth, E., Armour, K. C., Bitz, C. M. and DeWeaver, E. 2011. Persistence and inherent predictability of Arctic Sea ice in a GCM ensemble and observations. *J. Climate* **24**, 231–250.

Bretherton, C. S., Smith, C. and Wallace, J. M. 1992. An intercomparison of methods for finding coupled patterns in climate data. *J. Climate* **5**, 541–560.

Budikova, D. 2009. Role of Arctic sea ice in global atmospheric circulation: a review. *Globa.Planet. y Change* **68**, 149–163.

Cohen, J., Barlow, M., Kushner, P. J. and Saito, M. 2007. Stratosphere–Troposphere coupling and links with Eurasian land surface variability. *J. Climate* **20**, 5335–5343.

Dee, D. P. and Uppala, S. 2009. Variational bias correction of satellite radiance data in the ERA-interim reanalysis. *Q. J. R. Meteorol. Soc.* **135**, 1830–1841.

Deser, C., Tomas, R. A. and Peng, S. 2007. The transient atmospheric circulation response to north Atlantic SST and sea ice anomalies. *J. Climate* **20**, 4751–4767.

Dethloff, K., Rinke, A., Benkel, A., Køltzow, M., Sokolova, E. and co-authors. 2006. A dynamical link between the Arctic and the global climate system. *Geophys. Res. Lett.* **33**, L03703.

Francis, J. A., Chan, W., Leathers, D. J., Miller, J. R. and Veron, D. E. 2009. Winter Northern Hemisphere weather patterns remember summer Arctic sea-ice extent. *Geophys. Res. Lett.* **36**, L07503.

Gerdes, R. 2006. Atmospheric response to changes in Arctic sea ice thickness. *Geophys. Res. Lett.* **33**, L18709.

Graversen, R. G., Mauritsen, T., Tjernström, M., Källén, E. and Svensson, G. 2008a. Vertical structure of recent Arctic warming. *Nature* **451**, 53–56.

Graversen, R. G ,Mauritsen, T., Tjernström, M., Källén, E., and Svensson, G. 2008b. On-line supplement to 'Vertical structure of recent Arctic warming'. *Nature* **451**, 53–56. DOI:10.1038/ nature06502.

Honda, M., Inoue, J. and Yamane, S. 2009. Influence of low Arctic sea-ice minima on anomalously cold Eurasian winters. *Geophys. Res. Lett.* **36**, L08707.

Honda, M., Yamazaki, K., Tachibana, Y. and Takeuchi, K. 1996. Influence of Okhotsk sea-ice extent on atmospheric circulation. Geophys. *Res. Lett.* **23**, 3595–3598.

Inoue, J., Hori, M. E., Tachibana, Y. and Kikuchi, T. 2010. A polar low embedded in a blocking high over the Pacific Arctic. *Geophys. Res. Lett.* **37**, L14808.

Lindzen, R. S. and Farrell, B. 1980. A Simple Approximate result for the maximum growth rate of baroclinic instabilities. *J. Atmos. Sci.* **37**, 1648–1654.

Liu, Z. and Alexander, M. 2007. Atmospheric bridge, oceanic tunnel, and global climate teleconnections. *Rev. Geophys.* **45**, RG2005.

Overland, J. E. and Wang, M. 2010. Large-scale atmospheric circulation changes are associated with the recent loss of Arctic sea ice. *Tellus A* **62**, 1–9.

Petoukhov, V. and Semenov, V. A. 2010. A link between reduced Barents-Kara sea ice and cold winter extremes over northern continents. *J. Geophys. Res.* **115**, D21111.

Rayner, N. A., Parker, D. E., Horton, E. B., Folland, C. K., Alexander, L. V. and co-authors. 2003. Global analyses of sea surface temperature, sea ice, and night marine air temperature since the late nineteenth century. *J. Geophys. Res.* **108**, 4407.

Rigor, I. G., Wallace, J. M. and Colony, R. L. 2002. Response of sea ice to the Arctic oscillation. *J. Climate* **15**, 2648–2663.

Screen, J. A. and Simmonds, I. 2010. The central role of diminishing sea ice in recent Arctic temperature amplification. *Nature* **464**, 1334–1337.

Screen, J. A. and Simmonds, I. 2011. Erroneous Arctic temperature trends in the ERA-40 reanalysis: a closer look. *J. Climate* **24**, 2620–2627.

Sempf, M., Dethloff, K., Handorf, D. and Kurgansky, M. V. 2005. Idealized modeling of the northern annular mode: orographic and thermal impacts. Atmos. *Sci. Let.* **6**, 140–144.

Sempf, M., Dethloff, K., Handorf, D. and Kurgansky, M. V. 2007. Circulation regimes due to attractor merging in atmospheric models. *J. Atmos. Sci.* **64**, 2029–2044.

Serreze, M. C., Holland, M. M. and Stroeve, J. 2007. Perspectives on the Arctic's shrinking sea-ice cover. *Science* **315**, 1533–1536.

Sokolova, E., Dethloff, K., Rinke, A. and Benkel, A. 2007. Planetary and synoptic scale adjustment of the Arctic atmosphere to sea ice cover changes. *Geophys. Res. Lett.* **34**, L17816.

Stroeve, J. C., Holland, M. M., Meier, W., Scambos, T. and Serreze, M. C. 2007. Arctic sea ice decline: faster than forecast. *Geophys. Res. Lett.* **34**, L09501.

Stroeve, J. C., Serreze, M. C., Barrett, A. and Kindig, D. N. 2011a. Attribution of recent changes in autumn cyclone associated precipitation in the Arctic. *Tellus A* **63**, 653–663.

Stroeve, J. C., Serreze, M. C., Holland, M. M., Kay, J. E, Malanik, J. and co-authors. 2011b. The Arctic's rapidly shrinking sea ice cover: a research synthesis. *Climatic Change*, DOI: 10.1007/s10584-011-0101-1.

Tietsche, S., Notz, D., Jungclaus, J. H. and Marotzke, J. 2011. Recovery mechanisms of Arctic summer sea ice. *Geophys. Res. Lett.* **38**, L02707.

Trenberth, K. E. 1986. An assessment of the impact of transient eddies on the zonal flow during a blocking episode using localized Eliassen-Palm flux diagnostics. *J. Atmos. Sci.* **43**, 2070–2087.

von Storch, H. and Zwiers, F. W. 1999. Statistical Analysis in Climate Research. Cambridge University Press, 494 pp.

Appendix

The maximum Eady growth rate σ is calculated from daily mean ERA-Interim data following the approach by Lindzen and Farrell (1980):

$$\sigma = 0,3125 \frac{g}{TN} \left| \frac{dT}{dy} \right|.$$

Here, T is temperature, g is the gravitational acceleration and N is the Brunt-Väisälä frequency. Localized Eliassen-Palm fluxes (EP flux) are defined by Trenberth (1986). The calculation takes place in log-pressure coordinates $z^* = -H \ln(p/p_s)$, where p is pressure, p_s is pressure at the surface and $H = RT/g$ is the standard scale height with R the specific gas constant of air. The vector $\overrightarrow{E_u}$, whose divergence describes the zonal wind forcing, is derived as

$$\overrightarrow{E_u} = \left[\frac{1}{2} (\overline{v'^2} - \overline{u'^2}); -\overline{u'v'}; f \frac{\overline{v'T'}}{S} \right]$$

where u and v are the wind components in the zonal and meridional direction respectively, f is the Coriolis parameter and the vertical static stability $S = dT/dz^* + RT/(c_p H)$. An overbar represents a monthly mean, while a prime denotes the deviation from that mean. Both horizontal components in the EP flux vector are called the barotropic part, whereas the meridional and vertical components form the baroclinic portion. The divergence of the EP flux vector in spherical coordinates can be expressed as

$$\nabla \cdot \overrightarrow{E_u} = \frac{1}{2} \cos \varphi \frac{\partial}{\partial x} (\overline{v'^2} - \overline{u'^2}) - \frac{1}{\cos \varphi} \frac{\partial}{\partial y} (\overline{u'v'} \cos^2 \varphi)$$
$$+ f \cos \varphi \frac{1}{\rho} \frac{\partial}{\partial z^*} \left(\rho \frac{\overline{v'T'}}{S} \right).$$

The maximum covariance analysis (MCA; von Storch and Zwiers 1999) (often called somewhat misleading as singular value decomposition (SVD) analysis in the literature, Bretherton et al., 1992) is a statistical method for detecting coupled patterns between pairs of climate fields $\overrightarrow{X}(j,t)$, $j = 1 \ldots J_X, t = 1 \ldots T$ and $\overrightarrow{Y}(j,t), j = 1 \ldots J_Y, t = 1 \ldots T$. In the MCA framework, the anomaly fields $\overrightarrow{X'}(j,t)$ and $\overrightarrow{Y'}(j,t)$ are projected onto the spaces spanned by the MCA patterns $\overrightarrow{e_j}$ and $\overrightarrow{f_j}$:

$$\overrightarrow{X'} = \sum_{j=1}^{J_X} \alpha_j^X(t) \overrightarrow{e_j}$$

$$\overrightarrow{Y'} = \sum_{j=1}^{J_Y} \alpha_j^Y(t) \overrightarrow{f_j}$$

The orthonormal set of MCA patterns, $\overrightarrow{e_j}$ and $\overrightarrow{f_j}$, are determined by maximizing the covariance between the expansion coefficients $\alpha_j^X(t)$ and $\alpha_j^Y(t)$. This constrained optimization problem can be solved by calculating the eigenvalues and eigenvectors of the cross-covariance matrix between the two data fields. This eigenvalue problem may be solved by singular value decomposition. Before calculating the cross-covariance matrix, equal-area weighting is ensured by multiplying the fields with the square root of the cosine of latitude.